AGU PUBLICATIONS

JGR

Journal of Geophysical Research: Oceans

RESEARCH ARTICLE

10.1002/2014JC009900

Global and regional sea level change during the 20th century

Manfred Wenzel[1] and Jens Schröter[1]

[1]Helmholtz Centre for Polar and Marine Research, Alfred-Wegener-Institute, Bremerhaven, Germany

Key Points:
- Global mean sea level change since 1900: 1.77 mm yr^{-1}
- No significant acceleration for the global mean sea level
- Local accelerations between −0.1 and +0.1 mm yr^{-2}

Supporting Information:
- Readme
- List of selected tide gauges

Correspondence to:
M. Wenzel,
manfred.wenzel@awi.de

Citation:
Wenzel, M., and J. Schröter (2014), Global and regional sea level change during the 20th century, *J. Geophys. Res. Oceans*, *119*, 7493–7508, doi:10.1002/2014JC009900.

Received 11 FEB 2014
Accepted 10 SEP 2014
Accepted article online 19 SEP 2014
Published online 7 NOV 2014

Abstract Sea level variations prior to the launch of satellite altimeters are estimated by analyzing historic tide gauge records. Recently, a number of groups have reconstructed sea level by applying EOF techniques to fill missing observations. We complement this study with alternative methods. In a first step gaps in 178 records of sea level change are filled using the pattern recognition capabilities of artificial neural networks. Afterward satellite altimetry is used to extrapolate local sea level change to global fields. Patterns of sea level change are compared to prior studies. Global mean sea level change since 1900 is found to be 1.77 ± 0.38 mm yr^{-1} on average. Local trends are essentially positive with the highest values found in the western tropical Pacific and in the Indian Ocean east of Madagascar where it reaches about +6 mm yr^{-1}. Regions with negative trends are spotty with a minimum value of about −2 mm yr^{-1} south of the Aleutian Islands. Although the acceleration found for the global mean, +0.0042 ± 0.0092 mm yr^{-2}, is not significant, local values range from −0.1 mm yr^{-2} in the central Indian Ocean to +0.1 mm yr^{-2} in the western tropical Pacific and east of Japan. These extrema are associated with patterns of sea level change that differ significantly from the first half of the analyzed period (i.e., 1900–1950) to the second half (1950–2000). We take this as an indication of long period oceanic processes that are superimposed to the general sea level rise.

1. Introduction

When planning for the future sea level rise is one of the major concerns in predicting climate and climate change for the decades to come. Especially for people living in endangered coastal regions and on islands this is of vital importance. Projections for global sea level rise have been compiled in the IPCC third, the fourth, and the fifth assessment reports [*Church et al*., 2001; *Bindoff et al*., 2007; *Church et al*., 2013, respectively]. But still these projections vary substantially. It is important first to understand the magnitude and variability of the past sea level change before we can reduce the uncertainties in future development. By now there seems to be a consensus about the global mean sea level trend during the last century, but there is still a disagreement whether there is an acceleration in global sea level rise [*Church and White*, 2006; *Jevrejeva et al*., 2008; *Woodworth et al*., 2009; or *Church and White*, 2011] or not [*Wenzel and Schröter*, 2010; *Houston and Dean*, 2011; *Spada and Galassi*, 2012]. Furthermore, satellite altimetry, that is available since the last decades, has shown the large spatial dependence in the sea level variability not only for coastal areas but for the whole globe. Various authors, like, e.g., *Church et al*. [2004], *Church and White* [2011], *Hamlington et al*. [2012], *Meyssignac et al*. [2012], and others, have attempted to reconstruct this spatial-temporal variability for the last century and to estimate trends and accelerations. Mostly these attempts apply a variant of the approach introduced by *Church et al*. [2004]. This method estimates empirical orthogonal functions (EOF) from altimetry and reconstructs the corresponding principal components (PC) by a fit to a selected set of tide gauges, i.e., the method tries to reconstruct the tide gauge measurements by altimetry in the time derivative space. However, the sea level variations in the open ocean (altimetry) are to a large extent decoupled from the coastal zone (tide gauges) not only for the annual cycle but up to decadal time scales [*Prandi et al*., 2009; *Vinogradov and Ponte*, 2010; *Bingham and Hughes*, 2012; *Calafat et al*., 2012]. Furthermore, *Christiansen et al*. [2010] and recently *Calafat et al*. [2014] demonstrated that this method performs poorly in reconstructing the interannual variability, which limits the value of this approach. They also point out under which circumstances using a spatially constant field (EOF0) in the reconstruction is advisable.

In this paper, we will address the development of the global and the local sea level during the 20th century in a slightly, but essentially, different way. The global sea level anomaly fields are reconstructed from tide gauges (TG's) for the period 1900–2009 in a two step procedure: at first missing values in the time series of a selected set of TG's will be reconstructed. *Wenzel and Schröter* [2010] already demonstrated the

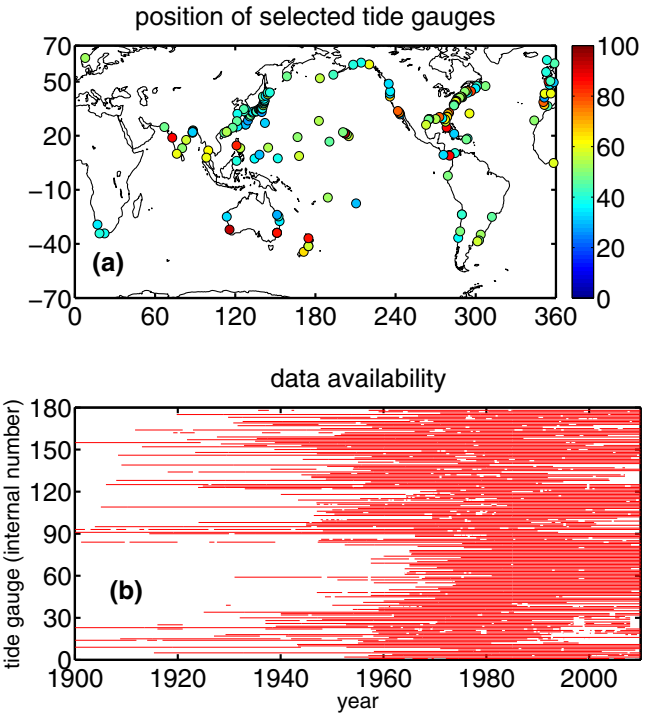

Figure 1. (a) Position of the selected tide gauges. The color shading gives the amount of available data in percent. (b) Data availability.

appropriateness of neural networks for this task. In *Wenzel and Schröter* [2010], the neural network used for gap filling was trained using only time steps without missing data. Here we will present an improved training procedure that can deal with arbitrarily distributed missing values even during the training phase. Sea level anomaly fields are then calculated from the thus completed TG records. This will be done by estimating their mapping onto the PC's of the EOF decomposition estimated from the altimetry data. In this way, our method differs from the conventional analysis used, e.g., by *Church et al.* [2004], *Church and White* [2006], and *Meyssignac et al.* [2012] in the way the PC's are estimated: those authors estimate them by fitting the weighted sum of altimetric sea level EOF's at the tide gauge positions, i.e., they try to reconstruct the tide gauges by means of the altimetry at these positions. The global sea level fields are then a desirable by-product. In contrast to this our focus is the reconstruction of the altimetry fields, i.e., we will be looking for a direct mapping of the tide gauge signal onto the PC's. This way, we alleviate problems of coastal amplification and decoupling. Afterward sea level change is calculated by combining the estimated PC's and the altimetric EOF's as it is performed conventionally.

2. Reconstruction of Tide Gauge Data

For our purpose, we selected the TG's in the latitudinal band 65°S–65°N from the Permanent Service for Mean Sea Level (PSMSL) data archive [*Woodworth and Player*, 2003] that have revised local reference (RLR) data and at least 30 annual mean values given. Thereof, we excluded all data from the Mediterranean Sea, the North Sea, the Baltic Sea, and the Sea of Japan. These areas have only a poor spatial representation in the altimetry data that will be used for reconstruction later on. Furthermore, semienclosed basins exhibit their own variability which is not representative for global scales. This selection finally gives 178 TG's listed in the supporting information and whose spatial distribution is shown in Figure 1 together with the availability of monthly data. It is obvious that many data are missing (approximately 50%) especially prior to 1950 and that there is no month at which measurements are available at all the selected TG's. However, a prerequisite for the method, that we will use later on to reconstruct the sea level fields, is to have a complete set of TG data at each time step. Thus, the first task should be to fill the data gaps in an eligible way. We will use a neural network for this purpose, whose applicability has been shown by *Wenzel and Schröter* [2010]. All computations to reconstruct the missing TG values will be done in the space of the monthly differences to avoid problems that may be caused by the different local reference frames. Furthermore, this makes the data more suitable for the neural network that has a value limiting characteristic (see below). Spikes, i.e., values that differs more than four standard deviations from the mean, are removed from the differentiated individual time series.

The neural network acts as a time stepping operator (backward in time) that has two time steps, n and $n-1$, at the input hindcasting time step $n-2$. While *Wenzel and Schröter* [2010] restricted the training of the network to examples that have three subsequent time steps without any missing data, we will introduce

an improved way to train the network that can use all available time steps. It is similar to the adjoint method used, e.g., in data assimilation and was inspired by reading the appendix in *Hsieh and Tang* [1998].

Details about the used "backpropagation" neural network can be found, e.g., in *Wenzel and Schröter* [2010] or *Hsieh and Tang* [1998]. Here we will give only a short description: a neural network is an artificial neural system, a computational model inspired by the notion of neurophysical processes. It consists of several processing elements called neurons, which are interconnected with each other exchanging information. In a backpropagation network, the neurons are ordered into layers: an input layer on the top, a hidden layer below and an output layer at the bottom. In addition to the neurons, there is a bias element in the input and the hidden layer that has no input but a constant unique output value. The information propagates forward through the network from the input to the hidden layer and then to the output. To manage this, each neuron (including the bias) of one layer is connected to every neuron in the underlying layer. They are not interconnected within the layers and there is no feedback. Each connection can be characterized by a certain connection strength or weight. The neurons of the input layer usually do only a scaling transformation on the input data, while the neurons in the following layers can be divided into two sections: an input section that sums the incoming signals from the overlying layer using the individual weights and a transfer/output section where the resulting signal is modified by a bistable transfer function $\mathcal{F}\{\}$, for which it is most common to use tanh $\{\}$. In our case, the total transfer function of the network used is given by:

$$\mathbf{y}_{n-2} = b_o + \mathbf{O} \cdot \tanh\left(b_h + \mathbf{H} \cdot \{\mathbf{x}_n, \mathbf{x}_{n-1}\}\right) \tag{1}$$

where $\mathbf{y}_{n-2}$ is the response of the network to the stimulus $\{\mathbf{x}_n, \mathbf{x}_{n-1}\}$, i.e., the TG information at time steps n and n − 1. b_h and b_o are the bias elements of the hidden and the output layer, respectively. **H** represents the transfer matrix (weights) from the input to the hidden layer and **O** from the hidden to the output layer.

With $\mathbf{d}_n = \{d_{n,k}\}$ being the vector of TG data at time step n and $\mathbf{y}_n = \{y_{n,k}\}$ the output of the neural network corresponding to that time step then the input $\mathbf{x}_n = \{x_{n,k}\}$ is given by:

$$x_{n,k} = \begin{cases} y_{n,k} & \text{if } d_{n,k} = undef/missing \\ d_{n,k} & \text{otherwise} \end{cases} \tag{2}$$

that is the input used for "predicting" time step n − 2 is composed of measured data at time steps n and n − 1. In case of missing measurements, they are replaced by previous estimates from the neural network. Because an "incorrect" input value at the time step n or n − 1 influences the hindcast for step n − 2, missing values at the initial time steps N and N − 1 can be estimated by the adjoint procedure. The dimensions of the input and the output layer are given by the number of selected TG's, i.e., there are 356 input and 178 output neurons. For the hidden layer, we will use 300 neurons. The unknown matrices **H**, **O**, and the bias elements b_h and b_h of the neural network as well as missing values in the initial conditions are estimated by minimizing the weighted least square costfunction **K**:

$$\mathbf{K} = \sum_n \sum_k w_{n,k} \left(y_{n,k} - d_{n,k}\right)^2 + c_r \cdot \left[\frac{n_{dat}}{n_h} \sum_i \sum_j \left(h_{i,j}\right)^2 + \frac{n_{dat}}{n_o} \sum_i \sum_j \left(o_{i,j}\right)^2\right] \tag{3}$$

that includes a ridge regression constraint weighted by c_r to minimize/suppress less important entries in the matrices. n_{dat} are the number of data points and n_h, n_o are the number of entries in the corresponding matrices **H** and **O**, respectively. Prior to applying the neural network the data of the individual TG are scaled to have a root-mean-square (RMS) value of one. This ensures that the entries in **H** and **O** are of the same order of magnitude, and the weights $w_{n,k}$ of the data misfit part in (3) can be set to one, i.e., we assume that all tide gauges have the same relative accuracy. As a final step, before estimating the sea level anomalies, the reconstructed TG monthly differences will be rescaled by multiplying with the RMS value used for scaling.

To estimate an optimal value for the weight c_r for the ridge regression constraint a subset of the data is excluded from the costfunction (3) for testing the performance of the network while scanning c_r in the range 0–1000. This scan is done for eight different sets of retained data (Figure 2). First, we used four disjunct sets of randomly chosen measurements (denoted R1–R4 in Figure 2). In the other four cases, the data

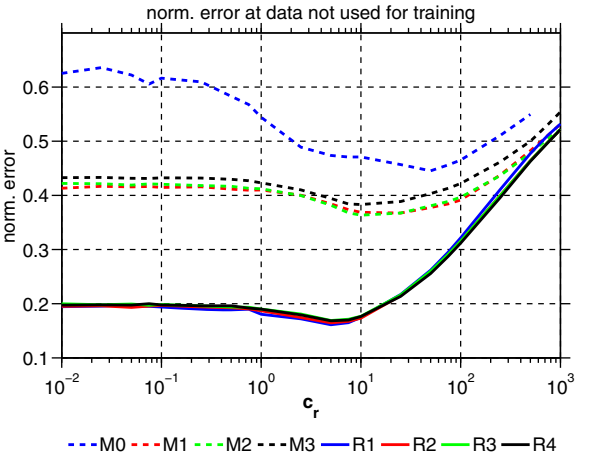

Figure 2. Remaining RMS error at data points not used for training depending on the chosen ridge regression value c_r. See text for details about the eight cases shown. The errors are normalized with their corresponding data RMS.

from different periods are retained completely. These periods are M0: [1900–1954]; M1: [1959–1964] and [1996–2001]; M2: [1966–1969], [1976–1979], and [1986–1989]; M3: [1971–1974], [1981–1984], and [1991–1994]. In all of the eight cases about 29,000 measurements, i.e., 25% of the available data, are kept for comparison. For each test case, the c_r value with minimum error at the data excluded from the training is identified (Figure 2) and the corresponding network is retrained using all available data. This finally gives eight realizations of the reconstructed scaled TG monthly differences, where the RMS error of the ensemble mean stays well between 5 and 18% of the signals RMS at the individual TG's with a mean of 10% (Figure 3a, black stems). Looking at the longer periods, i.e., after removing the annual cycle (Figure 3b), the relative RMS error is about twice as large. However, the strength of the annual cycle is about 10 times larger as the strength of the interannual signal. The correlation (Figure 3c) between the data and the reconstruction is well above 0.98 at all TG's. Even if the annual cycle is removed from both data sets there are only a few TG's where the correlation drops below 0.9 (Figure 3d). These are located mainly in Thailand and along the western North Pacific coast (China, Japan). A low-pass filter with a 1.5 years cutoff frequency is used to eliminate the annual cycle throughout this paper. The robustness of the results above is tested by the experiment MF (red diamonds

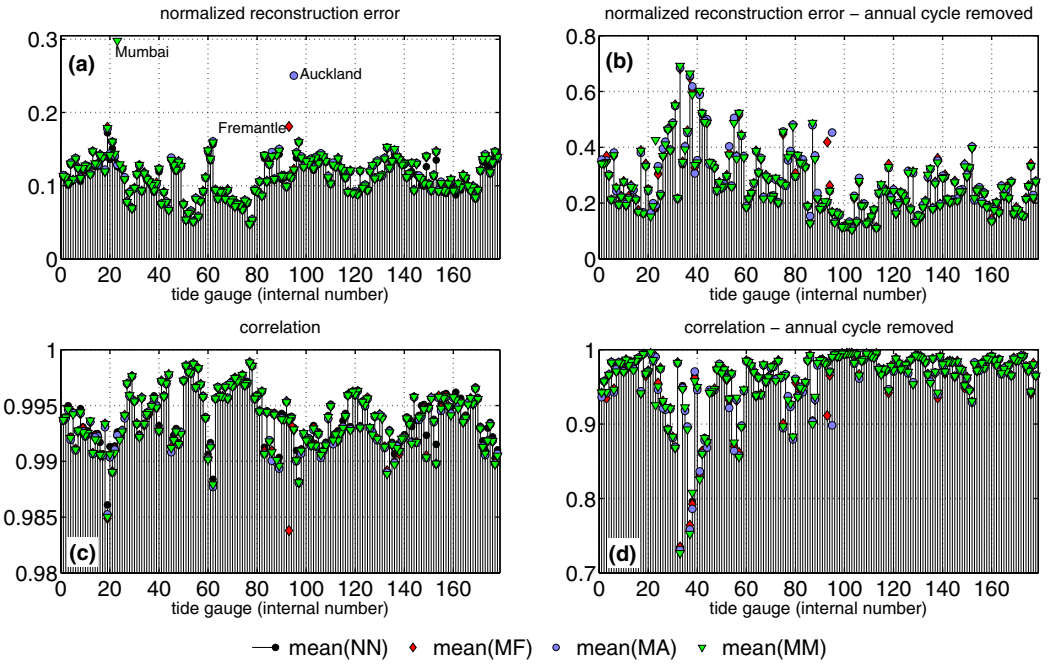

Figure 3. (a) Normalized RMS error of the reconstructed monthly sea level differences (ensemble mean) at the tide gauges compared to the PSMSL data. The error is normalized by the corresponding data RMS. (b) The same as Figure 3a, but after removing the annual cycle using a low-pass filter with a 1.5 years cutoff frequency. (c) Correlation between the reconstructed monthly sea level differences and the PSMSL data. (d) The same as Figure 3c, but for the low-pass filtered time series. The black stems, denoted mean(NN), are for the output of the trained neural networks using all available data. The red diamonds are the corresponding results from the control run MF. The corresponding control runs MM and MA are marked by the green triangles and the grayish-blue bullets, respectively. See the text for details about these control runs.

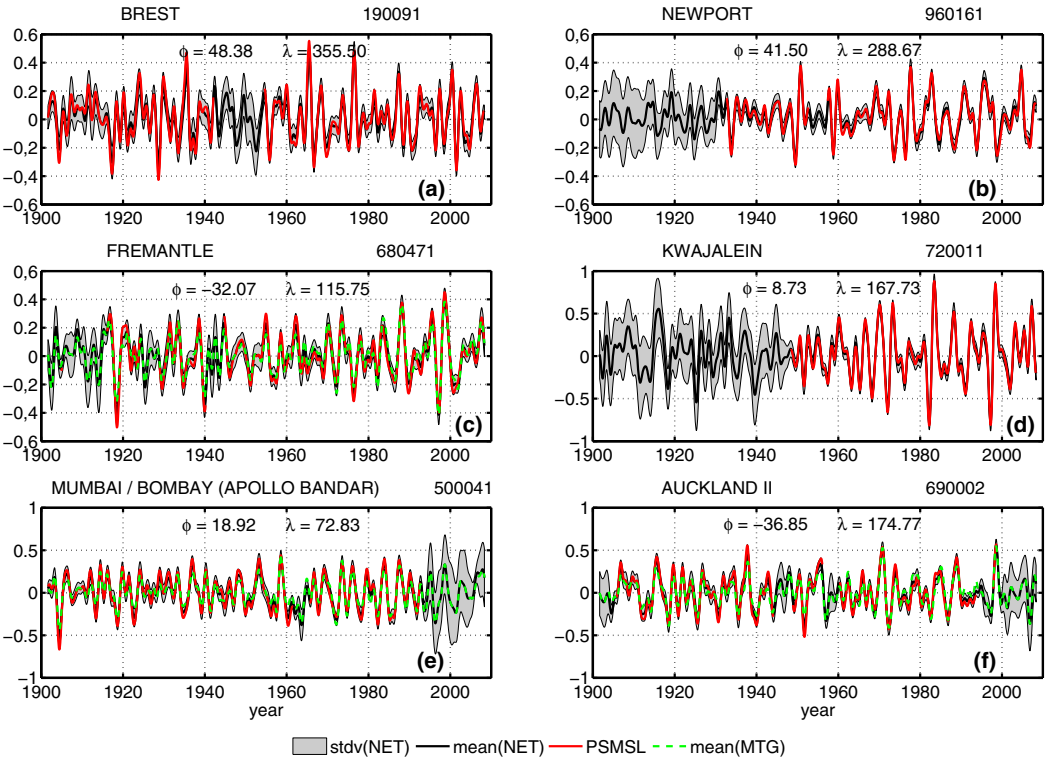

Figure 4. Ensemble mean of the reconstructed monthly sea level differences (scaled) at the tide gauges (a) Brest, (b) Newport, (c) Fremantle, (d) Kwajalein, (e) Mumbai, and (f) Auckland in comparison to the PSMSL data. For the sake of clearness, the time series are filtered to eliminate the annual cycle using a low-pass filter with a 1.5 years cutoff frequency. The gray shading in the back gives the corresponding ensemble spread (standard deviation). The dashed green lines denoted mean(MTG) in Figures 4c, 4e, and 4f are the results for the corresponding control runs MF, MM and MA, respectively (see text for details).

in Figure 3). In this experiment, the optimized networks are applied with the assumption that all data at Fremantle are unknown. The same test is done for Mumbai (denoted MM, green triangles) and Auckland (MA, grayish-blue bullets). As expected the quality of the reconstruction degrades for the corresponding tide gauge: the RMS errors nearly double and the correlations go down. Comparing the RMS errors and correlations for the unfiltered (Figures 3a and 3c) and the filtered time series (Figures 3b and 3d) shows that this deterioration mainly takes effect on the annual cycle. The results reveal also the influence on the nearby TG's as well as some teleconnections reaching as far as to the North Atlantic. However, there is only minor influence on most of the other TG's.

The ensemble mean and standard deviation of the reconstructed tide gauge time series (scaled monthly differences) are shown compared to the PSMSL data in Figure 4 for (a) Brest, (b) Newport, (c) Fremantle, (d) Kwajalein, (e) Mumbai, and (f) Auckland as examples. For the sake of clearness, these time series are filtered to eliminate the annual cycle using the same filter as above. The good correspondence between the ensemble mean and the data is already documented by Figure 3. However, it should be noted that the ensemble spread, that is small where data are available, grows with the length of the data gaps. The reconstructed tide gauge sea level (RTG = cumulative sum of the unscaled monthly differences) compared to the PSMSL data are shown in Figure 5 for the same TG's as in Figure 4. There are two versions of the RTG: in the first, denoted NET, the output from the neural net is used at all time steps and in the second one, denoted PSMSL+NET, the network output is inserted only where original data are missing. It is obvious from the figures that the neural network does not reproduce the PSMSL monthly differences exactly resulting in distinguishable time series for NET. However, these differences stay well within the ensemble spread of the reconstruction (light blue dashed lines) that is estimated after adjusting all time series to have a zero mean during the period overlapping with the altimetry data. For the version PSMSL+NET differences to the PSMSL data appear only at tide gauges that have gaps in between, like, e.g., Fremantle (Figure 5c) and especially Mumbai (Figure 5e). These differences are caused by the reconstructed values within the gaps that give a bridging slope different from the one in the PSMSL data. This becomes evident from looking at the

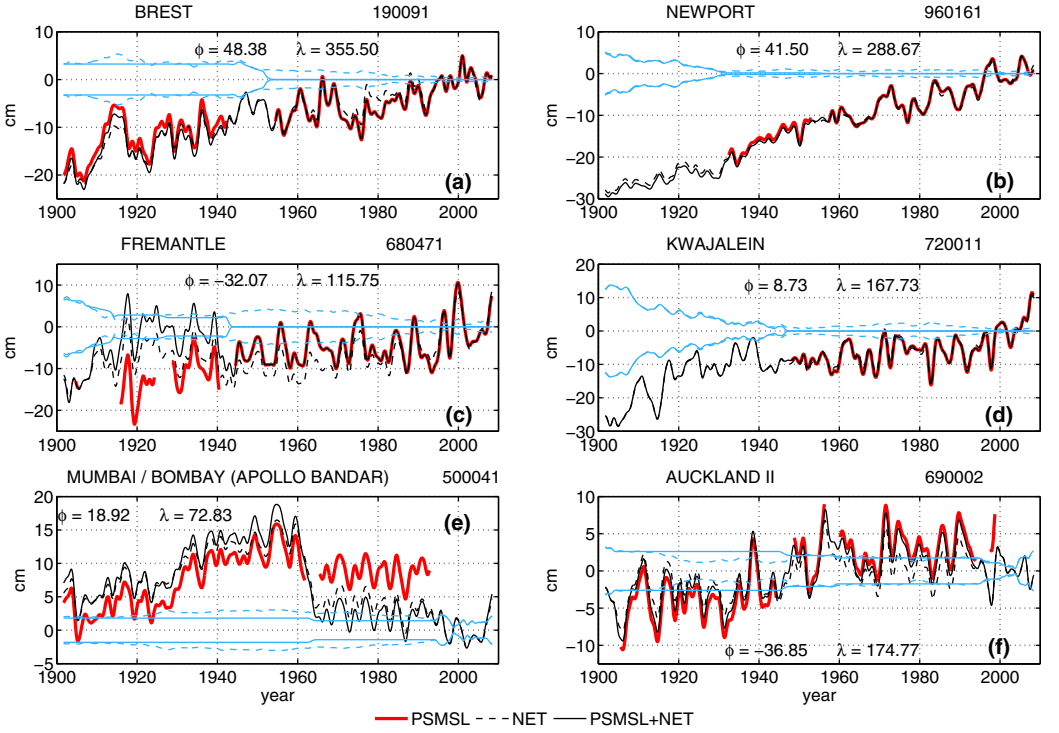

Figure 5. Ensemble mean of the reconstructed monthly sea level (RTG) at the tide gauges (a) Brest, (b) Newport, (c) Fremantle, (d) Kwajalein, (e) Mumbai, and (f) Auckland in comparison to the PSMSL data. There are two versions of RTG: in the first, denoted NET, the output from the neural net is used at all time steps (i.e., the cumulative sum from Figure 4) and in the second one, denoted PSMSL+NET, the network output is inserted only where original data are missing. For the sake of clearness, the time series are filtered to eliminate the annual cycle. The light blue curves give the corresponding ensemble spread (standard deviation).

data gap in 1963 at Mumbai (Figure 6). The values filling the gap in the monthly differences (Figure 6a) complement the annual cycle reasonably well. However, because all these values are negative, this results in an offset of about 7 cm in the sea level compared to the PSMSL data (Figure 6b). We will use PSMSL+NET in the following.

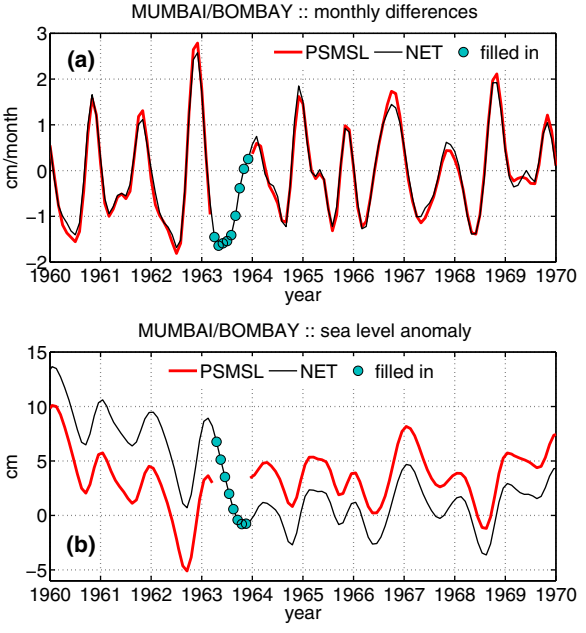

Figure 6. (a) Unfiltered and unscaled reconstructed monthly sea level differences at Mumbai during 1960–1970. (b) Reconstructed monthly sea level (unfiltered) at Mumbai during the same period. Note: the vertical adjustment of the sea level differs from Figure 5e.

3. Sea Level Reconstruction

3.1. Method

The global sea level anomaly fields for the period 1900–2009 will be reconstructed from the tide gauge data that were completed in the previous step using EOF decomposed satellite altimetry data. In this study, we will use the data taken from the CSIRO sea level web site (http://www.cmar.csiro.au/sealevel/sl_data_cmar.html) that are available from 1993 onward. The data from January 1993 to December 2010 will be

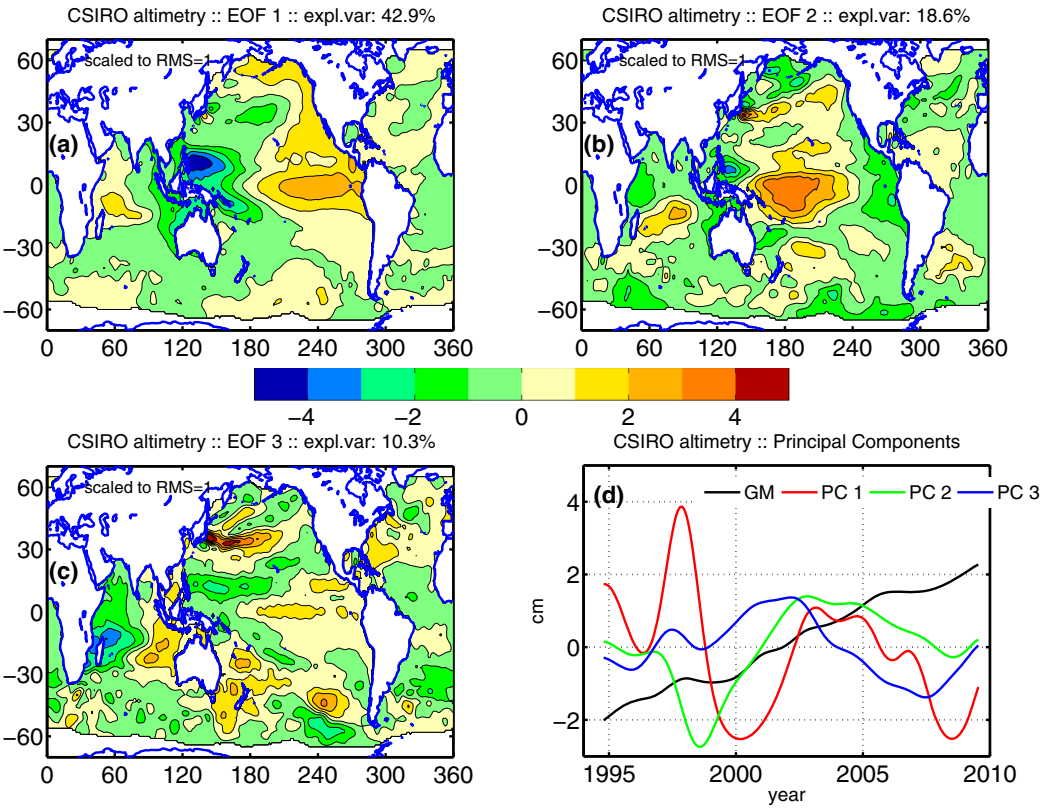

Figure 7. (a–c) The three leading EOF's from the filtered CSIRO altimetry data. The corresponding PC's are given in Figure 7d together with the global mean (GMSLA; black line) that was subtracted prior to the decomposition. Note: The EOF's are scaled to RMS = 1.0.

used in this paper. These data have a $1^\circ \times 1^\circ$ spatial and a monthly temporal resolution. To be consistent with the tide gauge measurements, we use the version with no inverse barometer correction applied (file: jb_ibn_srn_gtn_gin.nc; downloaded 3 May 2012).

In contrast to papers following the line of *Church et al*. [2004] and *Church and White* [2006], we will stay in the time domain to do the reconstruction, like, e.g., *Ray and Douglas* [2011]. For this a common reference, frame is needed for the tide gauges. While *Ray and Douglas* [2011] used only an ad hoc solution for this, the problem can be solved in our case by the following consideration: the altimetric sea level fields are anomalies to a certain mean dynamic topography. Because the tide gauge time series no longer have any missing data points, we can adjust their temporal mean value to the one of the corresponding altimetry data (nearest grid point) during the overlapping period. Thus, the tide gauges will be referenced to the same mean dynamic topography as the altimetry data. Indeed, this is implemented by setting the temporal mean to zero for both data sets. This changes only the effective mean dynamic topography but has no consequences for the temporal behavior. Therefore, the altimetry data are processed further as follows: (i) filter the local time series to exclude the annual cycle (1.5 years cutoff frequency), (ii) subtract the temporal mean field, and (iii) subtract the monthly global mean values (GMSLA). The latter can be regarded as the given zeroth PC of the following EOF decomposition. The EOF decomposition results in 23 EOF's, whereof 12 are needed to explain 98% of the variance. The first three EOF's are shown in Figures 7a–7c together with the corresponding PC's and the global mean (GMSLA; Figure 7d). The two leading EOF's/PC's clearly reflect the signals associated with the El Niño-Southern Oscillation (ENSO).

PC 1 to PC 12 plus the global mean (GMSLA) will be reconstructed from the accordingly filtered RTG data to derive global sea level anomaly fields from September 1901 to May 2008 (the other data are lost because of the filtering). In *Church et al*. [2004], *Church and White* [2006], or *Church and White* [2011], these PC's are estimated by fitting a weighted sum of EOF's to the existing TG values, i.e., they try to reconstruct the TG time series from the altimetry EOF's at the nearest grid point. In contrast to this, our focus is on the reconstruction of the altimetry fields, i.e., we are looking for a direct mapping of the tide gauge signal onto the PC's.

Table 1. Global Mean Sea Level Trend and Acceleration for 1900–2009 Resulting From Different Training Conditions Estimated by Fitting a Parabola $y=a+b(t-\bar{t})+c(t-\bar{t})^2$

	TV[a]	TE[b]	TC[c]	RR[d]	b = Trend (mm yr^{-1})	$2*c$= Acceleration (mm yr^{-2})
R1		No	No	Const.	1.60 ± 0.16	0.0028 ± 0.0048
R1E		Yes	No	Const.	1.92 ± 0.14	0.0018 ± 0.0048
R2E		Yes	No	$\sim r_l$	1.90 ± 0.10	0.0057 ± 0.0048
ACR1	PSMSL	No	ALT	Const.	1.61 ± 0.22	0.0023 ± 0.0094
ACR1E	+	Yes	ALT	Const.	1.91 ± 0.38	0.0072 ± 0.0140
ACR2E	NET	Yes	ALT	$\sim r_l$	1.91 ± 0.38	0.0069 ± 0.0136
GCR1		No	GIA	Const.	1.49 ± 0.18	0.0029 ± 0.0048
GCR1E		Yes	GIA	Const.	1.81 ± 0.14	0.0022 ± 0.0046
GCR2E		Yes	GIA	$\sim r_l$	1.78 ± 0.12	0.0063 ± 0.0046
Total mean:					1.77 ± 0.38	0.0042 ± 0.0092
Wenzel and Schröter [2010]:					1.56 ± 0.25	0.0016 ± 0.0043
Church and White [2011]:					1.7±0.2	0.009±0.004
Ray and Douglas [2011]:					1.70 ± 0.26	Not given

[a]TV: version of tide gauge reconstruction.
[b]TE: tide gauge error accounted for.
[c]TC: tide gauge trend correction: ALT = to altimeter trend; GIA = *Peltier* [2004].
[d]RR: ridge regression weights.

Thus, our procedure is more in the line of *Jevrejeva et al*. [2006] who estimated weights for the individual tide gauges to compute the global mean sea level. Each of these principal components, $\mathbf{pc}_k(t)$, will be reconstructed from the TG data matrix $\mathbf{TG}(t)$ directly by estimating a mapping vector $\mathbf{m}_k$ that provides:

$$\mathbf{pc}_k(t)=\mathbf{m}_k \cdot \mathbf{TG}(t) \tag{4}$$

wherein the subscript k gives the number of the PC. We do not look after the EOF's at this point, i.e., the PC values are the weighted sum of the TG values wherein the weights even might be negative. The vector $\mathbf{m}_k$ is estimated from the period where PC data exist via a least square fit minimizing the costfunction $\mathbf{J}$:

$$\mathbf{J}=\sum_n \left[pc_n-\sum_l m_l \cdot tg_{n,l}\right]^2+\sum_l g_l \cdot (m_l)^2 \tag{5}$$

consisting of a data misfit part (first sum on the right-hand side) and a ridge regression constraint (second part). Within (5) the subscript n denotes the time step and l the tide gauges. We dropped the numbering of the PC for simplicity. The minimization is done by using a conjugate gradient method. The ridge regression constraint is essential to damp the influence of the first guess on the solution, because the costfunction leads to a rank deficit system. There are only 164 data constraints (time steps), which might be linear dependent, to estimate 178 unknowns. Apart from the ridge regression constraint equations (4) and (5) describe a set of independent linear regressions from the TG's to the individual PC's. For the final sea level reconstruction, the estimated mapping vectors $\mathbf{m}_k$ (4) is assumed to be valid for the whole period September 1901 to May 2008.

Several estimates listed in Table 1 are made for each PC that differ in:

1. Whether or not errors in the tide gauge data are accounted for. In case of not accounting for errors only the ensemble mean of the TG reconstruction is used, otherwise all reconstruction ensemble members are utilized additionally, i.e., the data misfit part in (5) is made up of eight individual summands, one for each TG realization.
2. Whether or not a correction of the TG trend is applied to compensate the effect of vertical land movement (VLM) that does not affect altimetry. Either a correction toward the corresponding altimeter trend at the nearest grid point (ALT) is used following *Nerem and Mitchum* [2002] or a correction for the glacial isostatic adjustment (GIA) is applied using the estimates of *Peltier* [2004].
3. The choice of the weights g_l for the ridge regression constraint. They are set either to a constant value or to $g_l \sim r_l$. Herein, r_l is the RMS value of the individual RTG ensemble spread estimated from the whole period [1900–2010]. Thus, preferably the influence of TG's with a large uncertainty (= large data gaps) will be reduced/suppressed. In both cases, the weights are scales to $\sum g_l = N_T$, with N_T being the number of "training examples."

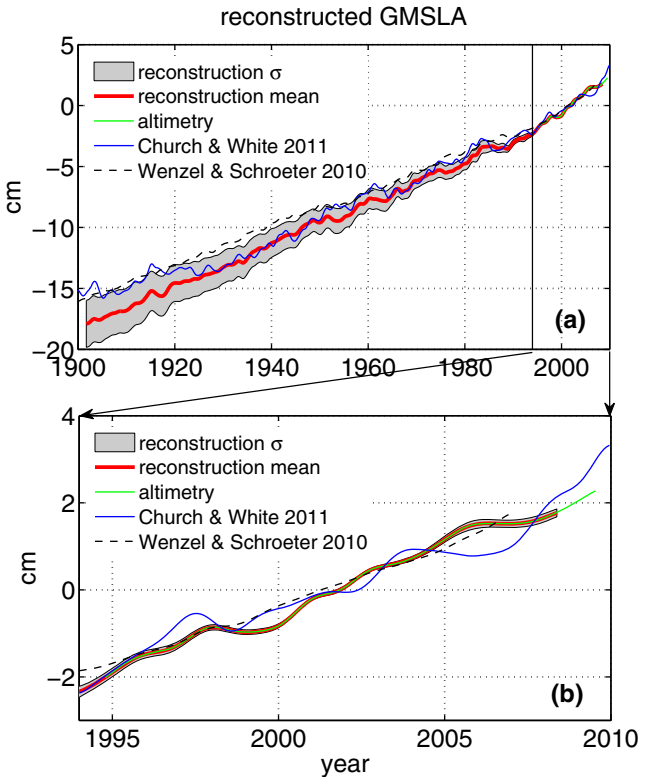

Figure 8. (a) Reconstructed global mean sea level anomaly. Shown is the mean from the nine training cases given in Table 1 together with their standard deviation σ. The results from *Wenzel and Schröter* [2010] and *Church and White* [2011] are included for comparison. (b) Cutout from Figure 8a for the period 1994–2010.

Considering all RTG reconstructions each of these estimates is given by an eight member ensemble, and the final ensembles of reconstructed GMSLA and PC's are composed of 72 members. Trends, accelerations, etc., will be estimated for every individual ensemble member, but only the mean of the appropriate (sub)ensemble will be discussed. Their errors will be estimated as twice the standard deviation of the corresponding ensemble. However, this makes it problematic to compare these errors to earlier estimates, e.g., from *Church and White* [2011] or others because the latter errors result from a single realization.

3.2. Global Mean Sea Level

The ensemble mean of the reconstructed global mean sea level anomalies (GMSLA) is shown in Figure 8 with its standard deviation, where the ensemble includes all nine PC reconstruction cases and all eight tide gauge realizations. The mean reconstruction shows only marginal deviations from the altimetry data (Figure 8b). On longer time scales, it compares also well to the earlier estimate of *Church and White* [2011]. Stronger deviations appear only prior to 1925. Likewise, the estimate of *Wenzel and Schröter* [2010] stays well at the upper one σ error bound of the ensemble. The mean centennial trend results to 1.77 ± 0.38 mm yr^{-1}, which consequently fits well to the trends given by *Wenzel and Schröter* [2010], *Church and White* [2011], or *Ray and Douglas* [2011]. The mean curve in Figure 8 appears as a relatively straight line with a nonsignificant positive acceleration of 0.0042 ± 0.0092 mm yr^{-2}. Although the mean acceleration is much stronger than the one given by *Wenzel and Schröter* [2010], it is still only approximately half the value of *Church and White* [2011]. However, a significant positive acceleration should not be expected before 2020–2030 according to the AR5 projections [*Haigh et al.*, 2014], unless the effect of internal climate variability is accounted for and removed [*Calafat and Chambers*, 2013]. More detailed information about the estimated GMSLA trend and acceleration from the single PC reconstruction cases are given in Table 1. As most commonly used these trends and accelerations are computed by fitting the quadratic regression line (QRL):

$$y = a + b \cdot (t - \bar{t}) + c \cdot (t - \bar{t})^2 \tag{6}$$

to the data, wherein $\bar{t}$ is the central time of the considered period. Then, the trend and the acceleration are given by the first and the second derivative of (6), respectively, evaluated at $t = \bar{t}$, i.e., the trend is given by b and the acceleration by $2c$.

The effect of the different training conditions on the trend can be summarized as follows: accounting for errors in the TG data increases the centennial trend of the GMSLA (in fact, an unrealistically strong increase of the noise/error level leads to a centennial GMSLA trend that approaches the trend prescribed by the altimetry data). Correcting the TG trends for VLM has only little influence but it differs with the choice of the correction: while using the ALT correction increases the GMSLA trend a bit, it is reduced when using GIA. However, the cases using ALT show by far the highest error bars especially when accounting for errors in the tide gauges. For the choice of the weights within the ridge regression constraint, we find a slight

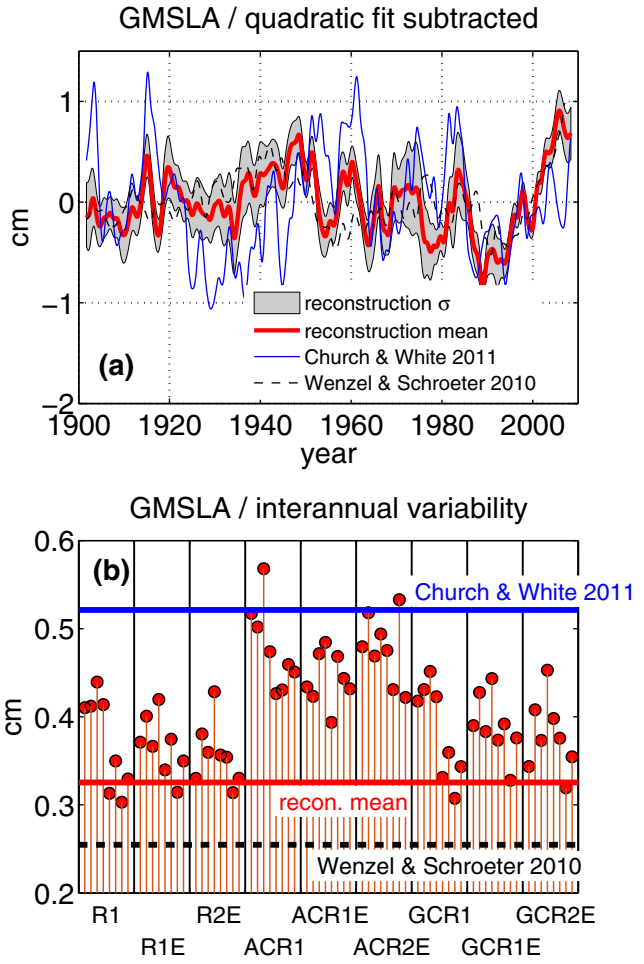

Figure 9. (a) Variability of the GMSLA after subtracting the corresponding quadratic regression line. The results from *Wenzel and Schröter* [2010] and *Church and White* [2011] are included for comparison. The standard deviation of these curves, shown in Figure 9b as horizontal lines, give a measure for the strength of the interannual variability. The red stems in Figure 9b represent the values for the individual realizations. Note: the red line indicates the standard deviation of the mean, not the mean of the individual standard deviations.

reduction of the GMSLA trend when reducing the influence of the most erroneous tide gauges (R2 cases, see Table 1 for details). This is consistent with the finding above, that an increase in the noise level also increases the centennial trend.

The effect on the acceleration is most dramatic when accounting for errors especially if the R2 condition (see Table 1) is applied, although the highest acceleration (0.0072 ± 0.0140 mm yr^{-2}) is found for case ACR1E (VLM correction: ALT, accounting for TG errors, constant regression weights), but still this value is lower than the one found by *Church and White* [2011]. In any case, only two of the accelerations are significantly different from zero on the two σ level: cases R2E (no VLM correction, accounting for errors, variable regression weights) and GCR2E (VLM correction: GIA, accounting for errors, variable regression weights).

The interannual variability of the GMSLA becomes evident when subtracting the corresponding QRL's (Figure 9a). For the reconstructions, the individual QRL is subtracted from each ensemble member separately, taking the mean and standard deviation afterward. Thus, variations originating from differences in the QRL's are removed. The interannual variability varies between -1 cm and $+1$ cm. It is slightly more intense than the one from *Wenzel and Schröter* [2010] but weaker than the one from *Church and White* [2011]. Furthermore, the similarities to the results of *Wenzel and Schröter* [2010] are stronger than to the ones compared to *Church and White* [2011], the corresponding correlations are 0.59 ± 0.04 and 0.28 ± 0.05, respectively. Taking the standard deviation of (GMSLA-QRL) as a measure of the strength of the interannual variability it is obvious from Figure 9b that the variability of the mean reconstruction is reduced by the averaging. The overwhelming majority of the single realizations show stronger variability, but each single value is still lower than the one obtained by *Church and White* [2011] except for two ensemble members. However, this does not discredit the present reconstruction as *Christiansen et al.* [2010] and *Calafat et al.* [2014] have shown that the method used by *Church and White* [2011] tend to overestimate the interannual variability. The best correlation (detrended time series) between the interannual variability of our GMSLA and a climate related index is found with the HadSST2 global mean [*Rayner et al.*, 2006], corr $= 0.37 \pm 0.06$, while only a negligible part can be explained by the extended multivariate ENSO index, MEI.ext [*Wolter and Timlin*, 2011], corr $= 0.16 \pm 0.06$. However, it is evident from Figure 7 that the variability related to the ENSO signal is most inherent in PC 1. Indeed the reconstructed PC 1 compares well to MEI.ext (Figure 10a) with a correlation (detrended) of corr $= 0.68 \pm 0.06$. Looking at shorter periods, e.g., a 15 years moving window (Figure 10b), the correlations are even higher, mainly above 0.9 except for the periods [1940–1950] and [1960–1970] where it drops down to 0.71 and 0.77, respectively.

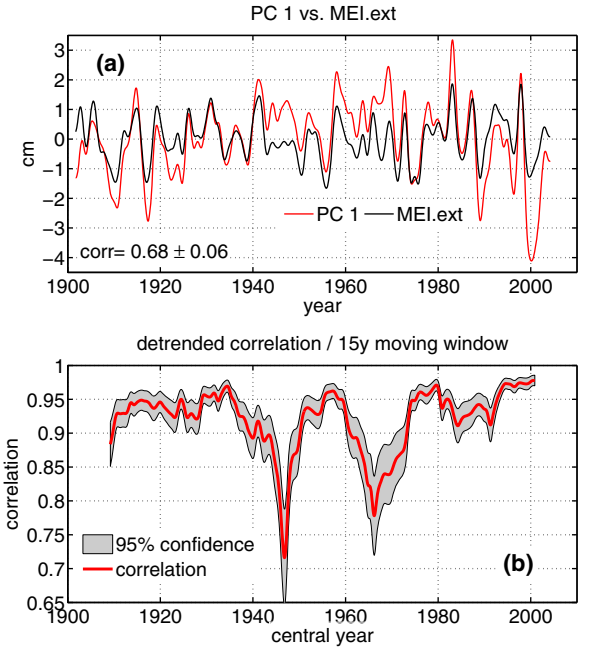

Figure 10. (a) Comparing the reconstructed PC 1 to the MEI.ext [*Wolter and Timlin*, 2011]. Both time series are detrended. (b) Correlation between PC 1 and MEI.ext in a 15 years moving window. Note: Both time series are detrended within each 15 years window separately before estimating the correlation.

3.3. Comparing to Tide Gauges

Although it was not the focus to reproduce the tide gauges when estimating the transfer vectors $\mathbf{m}_k$ it would be interesting how well the reconstructed sea level anomaly fits to the tide gauges. Using (4), the reconstructed sea level **RS** at the tide gauge positions (nearest grid point) is given by:

$$\mathbf{RS} = \mathbf{EOF}_{TG} \cdot \mathbf{PC} = \mathbf{EOF}_{TG} \cdot \mathbf{M} \cdot \mathbf{RTG} \quad (7)$$

wherein $\mathbf{EOF}_{TG}$ contains the values of the EOF's involved at the tide gauge positions and **M** is build from the transfer vectors $\mathbf{m}_k$. Figure 11 shows the **RS** for the same tide gauges as in Figure 5. The resulting **RS** appears relatively insensitive to whether it is estimated from the uncorrected **RTG** or from the ones corrected for VLM. A more detailed inspection showed that this is true for all 178 TG's. Furthermore, it is obvious that the quality of the correspondence between **RS** and **RTG** differs for the positions not only on short time scales but also on the longest, i.e., the centennial trend in this case. However, at least the latter should be similar, but they are not even if we compare to the trend corrected **RTG** (given as dashed lines in Figure 11 denoted as (RTG, ALT) and (RTG, GIA), respectively).

The differences of the centennial trends between **RS** and **RTG**, calculated as the linear fit to the time series **RS–RTG**, is illustrated in Figure 12. In Figure 12a, the mean of the nine reconstructed centennial trend differences is shown for all 178 stations as a bar plot. Their spatial distribution is also depicted in Figure 12b. We note a significant amplitude as well as spread for this difference which we expected to be small. We hesitate to call this difference an error as it obviously has a spatial structure similar to the trend corrections applied to the **RTG** prior to the estimate of the weighting matrix **M** (cases ACR1 to GCR2E in Table 1).

The GIA corrections, that are generally small, are depicted as red full circles in Figure 12a. If they coincide with the bar, we would have no difference between the reconstructed sea level **RS** trend and the GIA corrected TG trend. Clearly this is the case only for few stations. Notice the larger negative values for GIA along the East coast of the US (number 151 and above) but also for many Pacific islands (number 99–113) and part of the coast of Japan (47–82). Here the GIA is obviously beneficial, although not strong enough to explain the discrepancy.

Next, we consider the VLM correction to be given by the altimeter, ALT, represented as green diamonds in Figure 12a. This correction is approximately one order of magnitude stronger than GIA. It is based on much smaller timescales of only 20 years and includes many other processes and short term signals. Its spatial variations are much more pronounced. Applying ALT, we find good agreement with reconstructed estimates for a lot of stations. Most noticeable is the small difference along the US East coast but also for many Pacific islands (number 99–113) and part of the coast of Japan (47–82). On the other hand, we find several stations with very high discrepancies. As a conclusion, we have to say that for every type of correction we obtain very convincing examples of pro and con. Statistically, they perform equally bad. Based on these data for verification we can neither validate nor reject the reconstructed centennial trends.

Finally, we support our statement that the internal spread of the nine reconstructions is small by depicting min and max values at the stations as a read vertical line in Figure 12a. A histogram of this spread is shown in Figure 12c with a maximum around 1 and a median of 1.15 mm yr^{-1}. The spread is also the base for estimating the significance of the trend in the following figures. Trends in most areas exceed 1 mm yr^{-1}

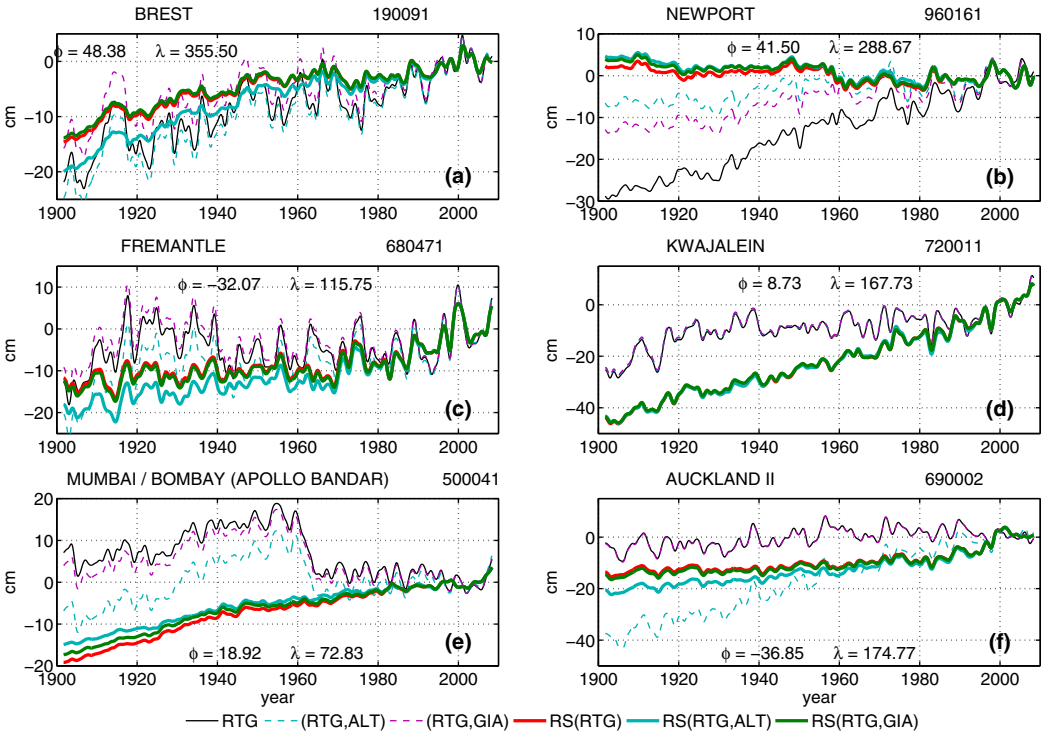

Figure 11. Comparing the reconstructed monthly tide gauge measurement RTG at (a) Brest, (b) Newport, (c) Fremantle, (d) Kwajalein, (e) Mumbai, and (f) Auckland to the reconstructed sea level RS at the nearest grid point. (RTG, ALT) and (RTG, GIA) are the ALT and GIA corrected tide gauge measurements, respectively.

making them significantly different from zero. Verification versus independent measurements still remains a problem. The difference to the verification data sets is as large as the difference between the verification data themselves. However, to better estimate relative land movement for the past hundred years is beyond the scope of this study.

3.4. Local Trends and Accelerations

Once the evolution of the global anomaly fields is estimated local trends (Figure 13) and accelerations (Figure 14) can be deduced. For the period [1994–2008] (Figure 13a) used to estimate **M** these trends are identical within plotting accuracy to the ones derived from altimetry. The centennial trend (Figure 13b) appears as a very smooth field with positive values nearly all over the ocean. Highest values are found in the western Pacific, up to 6 mm yr^{-1} in the tropical part, and in the Indian Ocean with the maximum east of Madagascar. Regions with negative trends are spotty with lowest values (-2 mm yr^{-1}) found south of the Aleutian Islands. These local trends are significant at the one σ error level of the nine member ensemble.

Looking at the 50 years trends for the periods [1901–1949] and [1950–1999] (Figures 13c and 13d, respectively) the fields show more spatial structure. As for the centennial trend, the fields are essentially positive and the global mean trends are approximately the same, 1.76 mm yr^{-1}, but the locations of the maxima are different for the single 50 years periods. Most prominent is the reduction of the trend in the tropical Indian Ocean from about 6 mm yr^{-1} in the first half of the century to 2 mm yr^{-1} in the second half. Furthermore, the sea level rise in the western part of the Pacific strengthens while in the eastern Pacific the positive trends turn to (not significant) negative values. In the Atlantic, the differences between the first and the second half of the century are not that pronounced.

In the Pacific, the centennial trend (Figure 13b) differs totally from the one of *Hamlington et al.* [2012], whose estimate is obviously dominated by their leading EOF. For the second half of the last century, one finds reasonable agreement of the estimated trend fields as compared to *Meyssignac et al.* [2012] except for the Indian Ocean, while there is only marginal conformance with *Hamlington et al.* [2011] or *Church et al.* [2004] and nearly no correspondence to *Ray and Douglas* [2011]. According to *Meyssignac et al.*

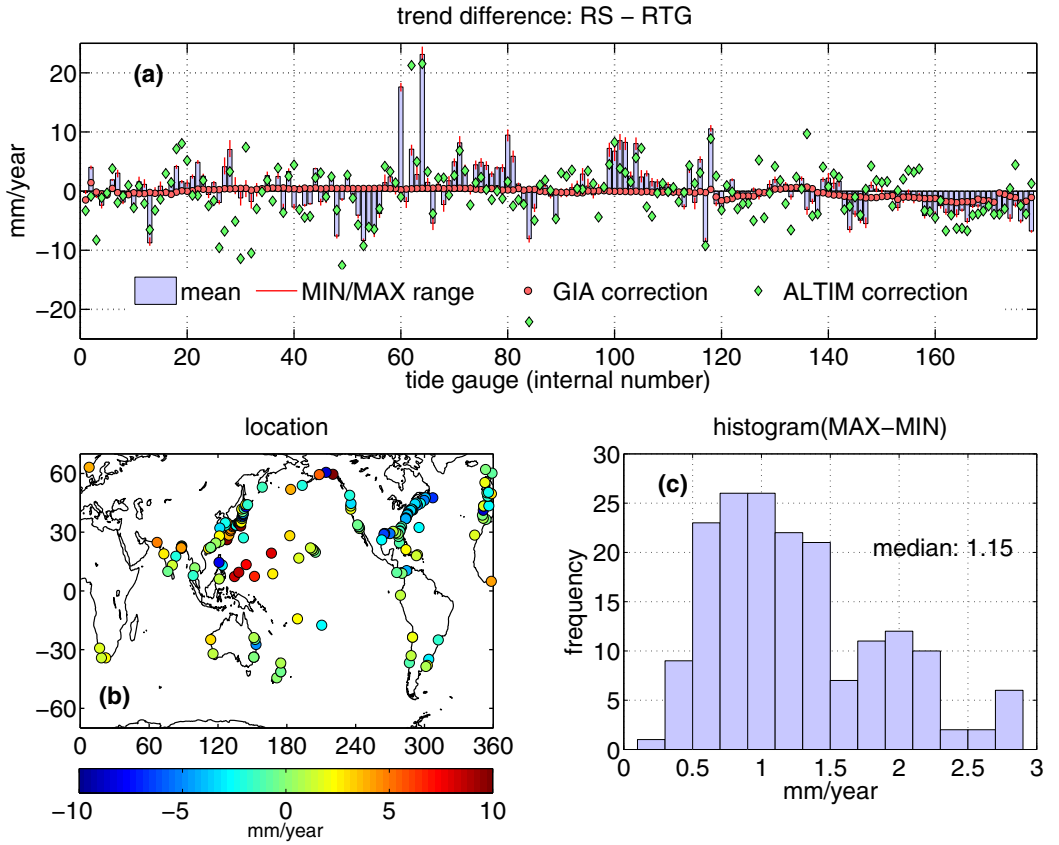

Figure 12. (a) The vertical bars give the difference of the centennial trend between the reconstructed local sea level RS (ensemble mean) and the data at all tide gauge locations. The small red lines represent the minimum-maximum range of this difference from the reconstruction ensemble. For comparison, the GIA (light red dots) and the ALT corrections (green diamonds) are included. (b) Regional distribution of the vertical bars in Figure 12a. (c) Histogram of the minimum-maximum range shown as vertical red lines in Figure 12a.

[2012], these differences might be a consequence of the divergent time span covered by the altimetry used to compute the EOF's and of the varying number of EOF's used for reconstruction, whereof the time span seems to be the most important factor [*Berge-Nguyen et al*., 2007]. Furthermore, the differences result at least in parts from the selection of the tide gauges and from the reconstruction of the sea level data as well.

Associated with the differences in the semicentennial trends (Figures 13c and 13d) is a clearly structured field of local accelerations and decelerations (Figure 14) that range from -0.11 mm yr^{-2} in the central Indian Ocean to $+0.10$ mm yr^{-2} off Japan and in the western tropical Pacific. This is opposite in sign to the *Woodworth et al*. [2009] analysis of the results from *Church and White* [2006] for large parts of the ocean. The global mean acceleration (0.0042 ± 0.0092 mm yr^{-2}) is two orders of magnitude lower and nonsignificant, although the temporal variability of the global mean SLA (Figure 9a) imply a sequence of higher valued accelerations and decelerations on shorter time scales.

4. Concluding Remarks

Sea level is first estimated at tide gauge positions for the full period 1900–2009. Data gaps are filled using neural network techniques. Comparing our estimates with data withheld during the gap filling process shows the skill of this type of reconstruction. Inevitably accuracy of the reconstructed values, measured by the spread of eight independent realizations, decreases with the gap length. For the beginning of the 20th century, the spread may even reach the signal strength for individual tide gauges. On the other hand, global sea level and other large scale variations are determined with much higher accuracy. They are based on a weighted average of all 178 tide gauge records. The standard deviation of this mean is much smaller than the mean of the standard deviations at tide gauges.

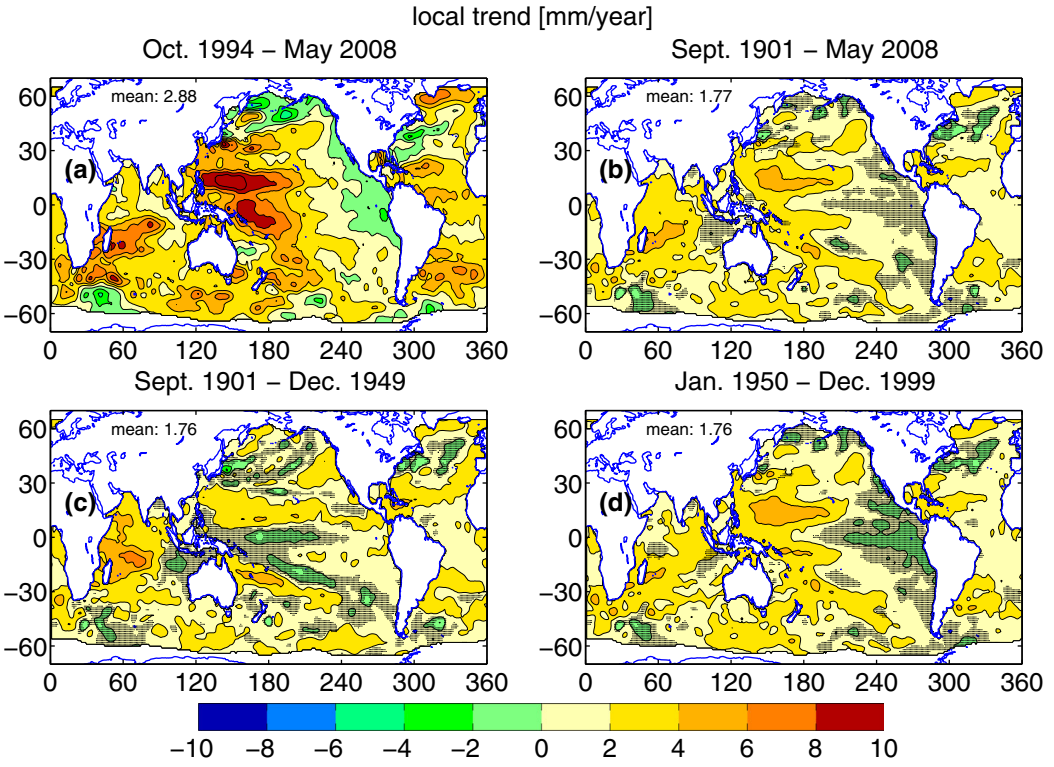

Figure 13. Reconstructed local sea level trend (mm yr^{-1}) for the periods (a) October 1994 to May 2008 coinciding with the altimetry data used, (b) September 1901 to May 2008, (c) September 1901 to December 1949, and (d) January 1950 to December 1999. Shown are the mean from the training cases given in Table 1. Areas with absolute values less than twice the corresponding standard deviations of the ensemble are dotted.

Comparing our global mean sea level reconstruction to earlier estimates, we observe a good agreement, but on local scale they differ more or less from the results, e.g., of *Church et al.* [2004] or *Hamlington et al.* [2011, 2012]. Thus, the question arises to what extent the extreme features appearing in the 50 years trend fields (Figures 13b and 13c) and in the acceleration (Figure 14) are artifacts of the method and/or the assumptions made. For instance, the importance of the time span used to compute the altimetry EOF's and of the numbers of EOF's used for reconstruction have been shown by *Berge-Nguyen et al.* [2007] or *Meyssignac et al.* [2012]. Similar caveats, of course, apply also for the selection of the tide gauges and the reconstructed sea level data, although we feel certain that our results are convincing. Especially at the beginning of the last century the majority of the used sea level data are reconstructed, and spurious teleconnections are easily generated when the behavior of global fields are estimated from regional limited measurements. Furthermore, the trend and the acceleration fields are indications of long period variability found, e.g., by *Woodworth et al.* [2009] in numerous tide gauges that obviously induced the 60 years oscillation in the reconstructed global mean sea level of *Church and White* [2011] and *Jevrejeva et al.* [2008] as reported by *Chambers et al.* [2012] or the even longer oscillations found by *Wenzel and Schröter* [2010] in the mean sea level of single ocean basins. This variability should be caused by changes in the oceanic

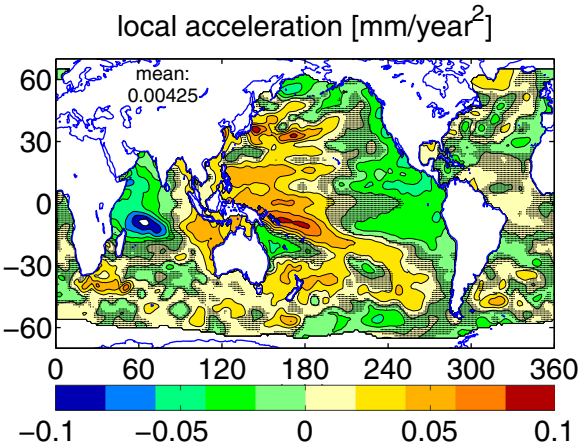

Figure 14. Reconstructed local sea level acceleration (mm yr^{-2}) for the period September 1901 to May 2008. Shown are the mean from the training cases given in Table 1. Areas with absolute values less than twice the corresponding standard deviations of the ensemble are dotted.

forcing fields and should have a feedback to them. It would be interesting to elaborate this in more detail, but this is beyond the scope of this study.

One problem remains, verification or rejection of the final results. All attempts to reconstruct past global sea level variations by combining altimetry and tide gauge records have to make corrections to place both types of measurement into the same reference frame. How this can be done best for past records remains an issue which needs attention.

Acknowledgments

The monthly mean tide gauge data and the corresponding GIA corrections [*Peltier*, 2004] used in this article were taken from the PSMSL data base. The utilized monthly fields of altimetric sea level anomalies are from the CSIRO sea level web page. The HadSST2 global mean was taken from http://www.cru.uea.ac.uk/cru/data/temperature/HadSST2-gl.dat and the MEI.ext data are from http://www.esrl.noaa.gov/psd/enso/mei.ext/table.ext.html. We greatly appreciate the public availability of these data sets. The reconstructed sea level anomaly fields **RS** described in this study are available in its EOF decomposed form from the PANGAEA data archive, http://doi.pangaea.de/10.1594/PANGAEA.832993. We value the constructive comments by three anonymous reviewers which helped to improve the manuscript and sharpen the focus of our study.

References

Berge-Nguyen, M., A. Cazenave, A. Lombard, W. Llovel, J. Viarre, and J. F. Cretaux (2007), Reconstruction of past decades sea level using thermosteric sea level, tide gauge, satellite altimetry and ocean reanalysis data, *Global Planet. Change*, *62*, 1–13, doi:10.1016/j.gloplacha.2007.11.007.

Bindoff, N. L., et al. (2007), Observations: Oceanic climate change and sea level, in *Climate Change 2007: The Physical Science Basis, Contribution of Working Group I to the Fourth Assessment Report of the Intergovernmental Panel on Climate Change*, edited by S. Solomon et al., pp. 385–432, Cambridge Univ. Press, Cambridge, U. K.

Bingham, R. J., and C. W. Hughes (2012), Local diagnostics to estimate density-induced sea level variations over topography and along coastlines, *J. Geophys. Res.*, *117*, C01013, doi:10.1029/2011JC007276.

Calafat, F. M., and D. P. Chambers (2013), Quantifying recent acceleration in sea level unrelated to internal climate variability, *Geophys. Res. Lett.*, *40*, 3661–3666, doi:10.1002/grl.50731.

Calafat, F. M., D. P. Chambers, and M. N. Tsimplis (2012), Mechanisms of decadal sea level variability in the eastern North Atlantic and the Mediterranean Sea, *J. Geophys. Res.*, *117*, C09022, doi:10.1029/2012JC008285.

Calafat, F. M., D. P. Chambers, and M. N. Tsimplis (2014), On the ability of global sea level reconstructions to determine trends and variability, *J. Geophys. Res. Oceans*, *119*, 1572–1592, doi:10.1002/2013JC009298.

Chambers, D. P., M. A. Merrifield, and R. S. Nerem (2012), Is there a 60-year oscillation in global mean sea level?, *Geophys. Res. Lett.*, *39*, L18607, doi:10.1029/2012GL052885.

Christiansen, B., T. Schmith, and P. Theill (2010), A surrogate ensemble study of sea level reconstructions, *J. Clim.*, *23*, 4306–4326.

Church, J. A., and N. J. White (2006), A 20th century acceleration in global sea-level rise, *Geophys. Res. Lett.*, *33*, L01602, doi:10.1029/2005GL024826.

Church, J. A., and N. J. White (2011), Sea-level rise from the late 19th to the early 21th century, *Surv. Geophys.*, *32*, 585–602, doi:10.1007/s10712-011-9119-1.

Church, J., J. Gregory, P. Huybrechts, M. Kuhn, K. Lambeck, M. Nhuan, D. Qin, and P. Woodworth (2001), Changes in sea level, in *Climate Change 2001: The Scientific Basis, Contributions of the Working Group I to the Third Assessment Report of the Intergovermental Panel on Climate Change*, edited by J. T. Houghton et al., pp. 641–684, Cambridge Univ. Press, N. Y.

Church, J. A., N. J. White, R. Coleman, K. Lambeck, and J. X. Mitrovica (2004), Estimates of the regional distribution of sea level rise over the 1950 to 2000 period, *J. Clim.*, *17*, 2609–2625.

Church, J., et al. (2013), Sea level change, in *Climate Change 2013: The Physical Science Basis, Contribution of Working Group I to the Fifth Assessment Report of the Intergovernmental Panel on Climate Change*, edited by T. Stocker et al., pp. 1137–1216, Cambridge Univ. Press, Cambridge, U. K.

Haigh, I. D., T. Wahl, E. J. Rohling, R. M. Price, C. B. Pattiaratchi, F. M. Calafat, and S. Dangendorf (2014), Timescales for detecting a significant acceleration in sea level rise, *Nat. Commun.*, *5*, 3635, doi:10.1038/ncomms4635.

Hamlington, B. D., R. R. Leben, R. S. Nerem, W. Han, and K.-Y. Kim (2011), Reconstructing sea level using cyclostationary empirical orthogonal functions, *J. Geophys. Res.*, *116*, C12015, doi:10.1029/2011JC007529.

Hamlington, B. D., R. R. Leben, and K.-Y. Kim (2012), Improving sea level reconstructions using non-sea level measurements, *J. Geophys. Res.*, *117*, C10025, doi:10.1029/2012JC008277.

Houston, J. R., and R. G. Dean (2011), Sea-level acceleration based on U.S. tide gauges and extensions of previous global-gauge analyses, *J. Coastal Res.*, *27*, 409–417, doi:10.2112/JCOASTRES-D-10-00157.1.

Hsieh, W. W., and B. Tang (1998), Applying neural network models to prediction and data analysis in meteorology and oceanography, *Bull. Am. Meteorol. Soc.*, *79*, 1855–1870.

Jevrejeva, S., A. Grinsted, J. C. Moore, and S. Holgate (2006), Nonlinear trends and multiyear cycles in sea level records, *J. Geophys. Res.*, *111*, C09012, doi:10.1029/2005JC003229.

Jevrejeva, S., J. C. Moore, A. Grinsted, and P. L. Woodworth (2008), Recent global sea level acceleration started over 200 years ago?, *Geophys. Res. Lett.*, *35*, L08715, doi:10.1029/2008GL033611.

Meyssignac, B., M. Becker, W. Llovel, and A. Cazenave (2012), An assessment of two-dimensional past sea level reconstructions over 1950–2009 based on tide-gauge data and different input sea level grids, *Surv. Geophys.*, *33*, 945–972, doi:10.1007/s10712-011-9171-x.

Nerem, R. S., and G. T. Mitchum (2002), Estimates of vertical crustal motion derived from differences of TOPEX/Poseidon and tide gauge sea level measurements, *Geophys. Res. Lett.*, *29*(19), 1934, doi:10.1029/2002GL015037.

Peltier, W. R. (2004), Global glacial isostasy and the surface of the ice-age earth: The ICE-5G(VM2) model and GRACE, *Ann. Rev. Earth. Planet. Sci.*, *32*, 111–149.

Prandi, P., A. Cazenave, and M. Becker (2009), Is coastal mean sea level rising faster than the global mean? A comparison between tide gauges and satellite altimetry over 1993–2007, *Geophys. Res. Lett.*, *36*, L05602, doi:10.1029/2008GL036564.

Ray, R. D., and B. C. Douglas (2011), Experiments in reconstructing twentieth-century sea levels, *Prog. Oceanogr.*, *91*(4), 496–515, doi:10.1016/j.pocean.2011.07.021.

Rayner, N. A., P. Brohan, D. E. Parker, C. K. Folland, J. J. Kennedy, M. Vanicek, T. Ansell, and S. F. B. Tett (2006), Improved analyses of changes and uncertainties in marine temperature measured in situ since the mid-nineteenth century: The HadSST2 dataset, *J. Clim.*, *19*, 446–469, doi:10.1175/JCLI3637.1.

Spada, G., and G. Galassi (2012), New estimates of secular sea level rise from tide gauge data and GIA modelling, *Geophys. J. Int.*, *191*(3), 1067–1094, doi:10.1111/j.1365-246X.2012.05663.x.

Vinogradov, S. V., and R. M. Ponte (2010), Annual cycle in coastal sea level from tide gauges and altimetry, *J. Geophys. Res.*, *115*, C04021, doi:10.1029/2009JC005767.

Wenzel, M., and J. Schröter (2010), Reconstruction of regional mean sea level anomalies from tide gauges using neural networks, *J. Geophys. Res.*, *115*, C08013, doi:10.1029/2009JC005630.

Wolter, K., and M. S. Timlin (2011), El Niño/Southern Oscillation behaviour since 1871 as diagnosed in an extended multivariate ENSO index (MEI.ext), *Int. J. Climatol.*, *31*, 1074–1087, doi:10.1002/joc.2336.

Woodworth, P. L., and R. Player (2003), The permanent service for mean sea level: An update to the 21st century, *J. Coastal Res.*, *19*, 287–295. [Available at http://www.psmsl.org.]

Woodworth, P. L., N. J. White, S. Jevrejeva, S. J. Holgate, J. A. Church, and W. R. Gehrels (2009), Evidence for the accelerations of sea level on multi-decade and century timescales, *Int. J. Climatol.*, *29*, 777–789, doi:10.1002/joc.1771.